Regional cytoarchitecture of the adult and developing mouse enteric nervous system

Ryan Hamnett[1,2,10], **Lori B. Dershowitz**[1,2,10], **Vandana Sampathkumar**[3,4], **Ziyue Wang**[5,6], **Julieta Gomez-Frittelli**[2,7], **Vincent De Andrade**[8], **Narayanan Kasthuri**[3,4], **Shaul Druckmann**[6,9], **Julia A. Kaltschmidt**[1,2,*]

[1]Department of Neurosurgery, Stanford University School of Medicine, Stanford, CA 94305 USA

[2]Wu Tsai Neurosciences Institute, Stanford University, Stanford, CA, 94305 USA

[3]Department of Neurobiology, University of Chicago, Chicago, IL 60637 USA

[4]Biosciences Division, Argonne National Laboratory, Lemont, IL 60439 USA

[5]Department of Applied Physics, Stanford University, Stanford, CA 94305 USA

[6]Department of Neurobiology, Stanford University, Stanford, CA 94305 USA

[7]Department of Chemical Engineering, Stanford University, Stanford, CA 94305 USA

[8]Advanced Photon Source, Argonne National Laboratory, Lemont, IL, 60439 USA

[9]Department of Psychiatry and Behavioral Sciences, Stanford University, Stanford, CA 94305 USA

[10]These authors contributed equally to this work

Summary

The organization and cellular composition of tissues are key determinants of their biological function. In the mammalian gastrointestinal (GI) tract, the enteric nervous system (ENS) intercalates between muscular and epithelial layers of the gut wall and can control GI function independent of central nervous system (CNS) input[1]. As in the CNS, distinct regions of the GI tract are highly specialized and support diverse functions, yet the regional and spatial organization of the ENS remain poorly characterized[2]. Cellular arrangements[3,4], circuit connectivity patterns[5,6] and diverse cell types[7–9] are known to underpin ENS functional complexity and GI function, but enteric neurons are most typically described only as a uniform meshwork of interconnected ganglia. Here, we present a bird's eye view of the mouse ENS,

*Corresponding author: jukalts@stanford.edu, Twitter handle: @kaltschmidt_lab, Lead Contact.

Declaration of interests: The authors declare no competing interests.

describing its previously underappreciated cytoarchitecture and regional variation. We visually and computationally demonstrate that enteric neurons are organized in circumferential neuronal stripes. This organization emerges gradually during the perinatal period, with neuronal stripe formation in the small intestine (SI) preceding that in the colon. The width of neuronal stripes varies throughout the length of the GI tract, and distinct neuronal subtypes differentially populate specific regions of the GI tract, with stark contrasts between SI and colon as well as within subregions of each. This characterization provides a blueprint for future understanding of region-specific GI function and identifying ENS structural correlates of diverse GI disorders.

eTOC blurb

The enteric nervous system spans the gastrointestinal (GI) tract and controls diverse GI functions, yet its structure is often characterized as a uniform meshwork. Hamnett et al. demonstrate that enteric neurons are organized into circumferential stripes that regionally differ in organization, development, and cellular composition.

Results

Neuronal organization in the adult ENS differs by region and plexus

Based on morphology and function, the adult mouse intestines can be broadly divided into 5 regions: duodenum, jejunum, ileum, proximal colon (PC), and distal colon (DC; Figure 1A). In all regions, enteric neurons are located within the myenteric plexus (MP), which controls motility, or the submucosal plexus (SMP), which regulates secretion and absorption (Figure 1A). To understand the broad layout of enteric neurons, we imaged large areas (up to ~50 mm^2) of both MP and SMP in each intestinal region of adult mice. Immunostaining neuron somas in the MP revealed circumferential orientation of ganglia, which loosely coalesced into a noncontinuous stripe pattern perpendicular to the longitudinal axis, herein referred to as neuronal stripes (Figures 1B,C and S1A). Submucosal ganglia of the small intestine (SI) did not show this arrangement, nor did they correlate with epithelial crypt organization (Figures S1B,C). In contrast, submucosal ganglia of the PC were organized into diagonal stripes, converging opposite the mesenteric border and aligning with mucosal folds (Figure 1D). These diagonal stripes were absent from DC SMP (Figure S1C).

Other regions of the gastrointestinal (GI) tract also showed myenteric ganglia organization, though not as parallel stripes (Figures S1D–F). In forestomach and glandular stomach, ganglia converged around the stomach towards the lesser curvature (Figures S1E–H). The few oesophageal neurons showed a weak diagonal orientation (Figure S1D).

Unlike neurons, glia are found throughout the muscle and epithelial layers in addition to neuronal plexuses (Figures S1I–L'). Within plexuses, glia tended toward the same organization as neurons, albeit with more frequent extra-ganglionic glia than neurons. Glial projections in the circular muscle showed a strong circumferential orientation (Figures S1I–J'), likely because of close apposition to neuron fibers (Figure S1M). Submucosal glia and their projections followed pathways between crypts (Figures S1K–L'). In PC SMP, the presence of many more extra-ganglionic glia masked the diagonal stripes so evident for

neurons (Figure S1L). However, this organizational difference between neurons and glia appeared limited to the PC SMP.

Full-thickness wholemount preparations of the intestines did not suggest any structural interplexus relationship and highlighted the orientation difference between the MP and SMP in the PC (Figure 1E). MP stripe formations emerged as peaks in longitudinal axis signal intensity profiles of wholemount images, which also confirmed the lack of circumferential structure in the SMP (Figure 1F). We confirmed this ENS organization using a separate imaging approach, synchrotron source X-ray tomography that allows simultaneous visualization of multiple cell types of both MP and SMP (Figures 1G,H). Taken together, the MP, but not the SMP, displays a striped neuronal architecture.

We next sought to characterize and quantify this region- and plexus-specific ENS structure. While intensity profiles (Figure 1F) are useful visualizations, they cannot reveal any structure not perpendicular to the x-axis, such as in PC SMP, and they are susceptible to tissue distortions. We therefore used conditional intensity function (CIF) plots to generate spatial probability maps of neuronal locations relative to a given neuron (Figure 1I; see Methods). An average neuron was always situated within a stripe flanked by higher order stripes, clearly displayed when the CIF is collapsed into a two-dimensional (2D) graph (Figure 1I, bottom). The PC contained the thickest stripes (Figure 1J), while the largest interstripe distances existed in the SI (Figure 1K). Myenteric neurons were densest in the PC and sparsest in the duodenum (Figure 1L). We found no sex-related differences (Figures S1N–P). Neuronal density was also different between stomach regions, while the oesophagus was the sparsest populated region overall (Figure S1Q). Glial density closely followed neuronal density (Figures S1R,S).

SMP neurons were sparser than myenteric neurons, and, in contrast to the MP, the densest SMP region was the duodenum (Figure 1M). Further, individual SMP ganglia tended to have a circumferential orientation, but only the PC exhibited any macrostructure beyond ganglia organization in the SMP (Figure 1N). Therefore, organization of enteric neurons and glia quantitatively and qualitatively differs between regions and plexuses of the GI tract.

Myenteric organization emerges progressively in a regionally specific manner

To assess how neuronal stripes arise, we visualized myenteric neurons in wholemount preparations from late embryonic through neonatal ages (Figures 2A and S2A). At embryonic day (E)14.5, when enteric neurons first populate the entire length of the mouse intestines[10], neurons were scattered throughout the SI and colon (Figures 2A). Beginning at E16.5 in the jejunum and E18.5 in the DC, scattered neurons reorganized into circumferential neuronal stripes, which resolved into individual ganglia postnatally (Figures 2A). CIF analysis confirmed the gradual emergence of neuronal stripes in the developing MP and differing organizational timelines between SI and colon (Figure 2B). To quantify this progressive organization, we compared nearest-neighbor distances of HuC/D-positive neurons to synthetically generated data with an imposed minimum nearest-neighbor distance of 10 μm, approximately the diameter of an enteric neuron (Figure 2C). At E14.5, the dispersion of neurons did not differ compared to random distributions; this dispersion transitioned to highly clustered at E16.5 in the duodenum and jejunum, at E18.5 in the

ileum, and at early postnatal stages in the colon (Figure 2D). Thus, neuronal stripes arise from a gradual reorganization of myenteric neurons, which occurs embryonically in the more proximal intestines and neonatally in the more distal intestines.

We next assessed whether gut growth and neuronal cell death contribute to the emergence of neuronal stripes. Intestinal length increased 10-fold between E14.5 and postnatal day (P)21, which correlated with decreased neuronal density and increased interstripe distance (Figures 2E–J and S2B–G). We used the apoptotic marker Caspase-3 to identify apoptotic neurons but detected only sparse labelling in the developing MP across region and development (Figure 2K,L). Collectively, these results suggest that intestinal growth, but not neuronal cell death, may influence organization of the developing MP.

Neuronal subtype distribution varies by intestinal region

We next sought to assess regional distribution of neuronal subtypes, focusing on known determinants of subtype function, such as calcium binding protein (CBP; Figures 3A–C), neurotransmitter (Figures 3D–I), and neuropeptide (Figures 3J–N) expression[11–13]. We observed differences in relative marker expression both between the SI and colon, and between regions within each. We found that markers attributed to a particular neuronal functional subtype tended to have similar regional distributions. For instance, markers representing excitatory motor neurons, including calretinin (Figures 3A and S3A), choline acetyltransferase(ChAT)-GFP (Figures 3D and S3D,M) and Tachykinin precursor 1(Tac1)Cre-tdT (Figures 3J and S4F), tended to decrease in expression from proximal to distal, with highest expression in the duodenum and lowest in the colon, although this was not significant for Tac1Cre-tdT. ChAT-GFP had the highest expression of any marker, present in 42–75% of neurons, depending on region (Figure 3D').

In contrast to excitatory motor neurons, expression of inhibitory motor neuron markers tended to increase distally. nNOS (Figures 3E and S3E) showed a non-significant trend of increasing expression from duodenum to DC, and vasoactive intestinal peptide(Vip)Cre-tdT (Figures 3L and S4C,I) was highest in the DC.

Secretagogin, a marker of a currently undefined subtype, showed a similarly shaped profile to VipCre-tdT (Figure 3C'), with approximately twice as many secretagogin neurons in the DC (~20%) compared to the SI (~11%) and PC (~9%)(Figures 3C and S3C). Secretagogin labelling also revealed qualitatively different fiber characteristics depending on region. In the SI, secretagogin fibers were restricted to interganglionic tracts, but fibers additionally innervated longitudinal and circular muscle in the PC and DC, respectively (Figures 3C and S3C). This may suggest as yet uncharacterized regionally-specific functions for secretagogin neurons.

Calbindin 1(Calb1)Cre-tdT (Figures 3B and S3B,J) and 5-hydroxytryptamine (5-HT; Figures 3H and S3H) both showed expression peaks in the duodenum and the PC. 5-HT and Calb1Cre-tdT fibers were restricted to the MP, consistent with their posited interneuron and sensory neuron identities, respectively. This fiber localization was also observed for vesicular glutamate transporter 2(VGLUT2)Cre-tdT (Figures 3F and S3F,K), a potential interneuron or sensory neuron marker. VGLUT2Cre-tdT expression was highest in the PC

(6%), almost 3-fold higher than in the ileum, though it lacked the duodenal peak of 5-HT or Calb1Cre-tdT (Figure 3F'). VGLUT2Cre-tdT was the only marker more highly expressed in both colonic regions than any SI region. Somatostatin, another interneuron marker, also showed highly significant enrichment in the PC (~13%), ~4-fold higher than in the ileum and DC (~3%)(Figures 3M,M' and S4D).

Two markers showed pronounced enrichment in the ileum: glutamate decarboxylase 2(Gad2)Cre-tdT (Figures 3G and S3G,L) and pituitary adenylate-cyclase-activating polypeptide(Pacap)Cre-tdT (Figures 3N and S4E). PacapCre-tdT expression was widespread, ranging from 20% (duodenum) to 40% (ileum). Despite its posited function as a motor neuron marker, we observed few muscle-innervating fibers, thus PACAP may have additional roles beyond its suggested motor neuron function. Tyrosine hydroxylase (TH; Figures 3I and S3I), labelling <1% of neurons, also peaked in the ileum, albeit with comparable levels in the jejunum and PC. Only proenkephalin(Penk)Cre-tdT (Figures 3K and S4B,G), expressed in both excitatory motor and interneurons, showed enrichment in the jejunum, though this was not significant.

In addition to neuronal expression, several markers were found in non-neuronal cells. PenkCre-tdT was present in diverse cell types including suspected immune cells and fibroblasts, which was supported by IHC against enkephalin (Figure S4H). PacapCre-tdT was expressed in glia and could be observed alongside neuronal expression within the same ganglion (Figure 3N, PC). Finally, Tac1Cre-tdT (Figure S4F) and Gad2Cre-tdT (Figure S3G, jejunum) also showed limited non-neuronal expression.

Within-region organization of neuronal subtypes is regular across neuronal stripes

We next examined neuronal subtype representation across myenteric neuronal stripes. We selected 4 markers covering a range of different cell types: motor neurons (VipCre-tdT[14] and calretinin[15]), sensory neurons (Calb1Cre-tdT[16]) and interneurons (somatostatin[17]) (Figures 4A–D). Within enteric neuronal stripes, the proportion of neurons positive for a given marker broadly reflected that of the entire region, and these distributions shifted appropriately between regions. For instance, calretinin marked 35% of ileum neurons overall (Figure 3A'), and individual stripes contained 15–60% calretinin neurons, with a peak at ~35% (Figure 4A). Subtypes were well distributed across stripes, with few stripes containing zero neurons of a given subtype unless that marker was very sparsely expressed, such as ileal somatostatin (Figures 3M,4D). This was further illustrated when comparing longitudinal axis intensity profiles of HuC/D signal with that of a given subtype (Figures 4E and S4J,K). Only at very low subtype expression did the correlation between profiles vanish, such as in ileal but not colonic somatostatin (Figure 4E). There was a strong link between the Pearson r value and the percentage of neurons positive for a given marker (Figure 4F). Therefore, even with a restricted area of analysis (1800 μm^2), a subtype's prevalence can be relatively low (e.g. 5%), yet its spatial distribution within a region can reflect that of HuC/D, providing evidence for an approximately even subtype distribution across enteric neuronal stripes.

Discussion

By combining large-scale image analysis with computational methods over multiple regions and ages of the mouse intestines, we demonstrate that the mouse MP possesses a gross cytoarchitecture of circumferential neuronal stripes that regionally differ in organization, development, and neuronal composition. Further, our computational approach for spatial analysis provides a new tool to describe and quantify patterning across tissues and organisms.

The role of individual neuronal stripes remains to be elucidated, though structural differences seen between regions likely contribute to the particular functions of SI and colon. Clonally related ENS cells inhabit overlapping domains and exhibit coordinated activity[18]; whether these functional units map onto the macrostructure of neuronal stripes has yet to be explored. Further, neuronal stripes could control rings of circular muscle, which possess the same orientation as neuronal stripes, or coordinate multiple longitudinal interneuron projections perpendicular to the stripes[19].

Another outstanding question regards the mechanisms underlying stripe development. We demonstrate that neuronal stripes emerge earlier in the proximal than in the distal intestines, which correlates with the timing of neural crest cell (NCC) colonization[20]. The ENS arises from two populations of NCCs. In mouse, vagal NCCs enter the proximal intestines at E8.5 and migrate distally[21]; sacral NCCs enter the distal intestines at E13.5 and migrate proximally[22]. Their final locations and extent of overlap remain unknown and may contribute to structural, developmental, and subtype distribution differences among GI regions.

Both cell autonomous and non-cell autonomous mechanisms may influence ENS structural development. In chick embryos, reduction of vagal NCCs below a critical value results in aganglionic regions of intestine[23], and inhibition of NCC apoptosis increases ENS cell number[24]. Additionally, work in mice has shown that genetic manipulation of enteric neuron precursors, including the removal of the cell adhesion molecule β1 integrin[4] or the DNA-binding protein Hand2[3], disrupts MP structural development.

The role of non-neuronal tissues in ENS structural development is only partially understood. Studies in both chick and mouse suggest that intestinal vasculature is not required for normal intestine colonization by NCCs[25], and the organization of intestinal vasculature does not correlate with MP structure in the adult mouse ENS[26]. However, emerging evidence suggests that smooth muscle may influence ENS structural development, also supported by our observations of neuron organization in the stomach and oesophagus. In chick, the circular muscle differentiates just before the arrival of NCCs[27,28], and inhibition of circular muscle contractions changes the anisotropy of the embryonic chick ENS[29]. Both mechanical forces and morphogens influence intestinal smooth muscle orientation during development[28], and whether these factors affect neuronal stripe development and patterning has yet to be explored. Such mechanistic insights will not only improve our understanding of ENS development *in vivo* but will also be useful for generating intestinal organoids,

examples of which have two ENS plexuses but lack patterning along the longitudinal axis[30,31].

Our analysis of enteric neuron subtypes throughout the intestines reveals striking differences in distribution for many neurotransmitters, neuropeptides and CBPs across intestinal regions and neuronal stripes. Regional differences in neuronal marker distribution have been observed previously[9,32], and such differences are perhaps unsurprising, considering the specific functions of the SI, colon and subregions thereof, and regional differences in extrinsic ENS innervation[33–36]. Despite this, few studies have specifically investigated regionality, with many focusing on the ileum[37] or pooling entire organs[8]. Only recently have studies begun to examine regional differences, particularly between the PC and DC[5,9,26], where we also see strongly contrasting cytoarchitecture and subtype distributions. The functional relevance of regional expression profiles has been determined for some markers, such as Sst, which is regulated by the microbiome and is more prevalent in areas of increased microbiotal load[38]. The proportion of VGLUT2-positive cells is also sensitive to the ileal microbiome[39], but the importance of its increased levels down the length of the colon awaits determination. The functional significance of other distribution profiles, such as high 5-HT expression in the duodenum or peak VIP expression in the distal colon, remain to be elucidated.

Notwithstanding regionality, the proportion of enteric neurons that we observe expressing given markers, such as ChAT, nNOS, calretinin, TH and somatostatin, are comparable with prior immunolabelling and RNAseq studies of enteric cell types[7–9,38,40,41]. Genetic reporter lines allow for unambiguous counting of marker expression in cases where the native protein is not localized to the soma, including Substance P (Tac1Cre) and enkephalin (PenkCre), without the need for pharmacological agents such as colchicine. This allows clarification for populations found to have different expression levels in distinct studies. For example, reports of the proportion of enkephalin neurons range from 6–23%[7,42]. In PenkCre-tdT mice, we found that 21–30% of neurons were Penk-positive, depending on intestinal region, values supported by RNAseq studies, in which Penk is found across several subtype clusters[8,9]. There are also diverging reports on the extent of calbindin expression, a putative sensory neuron marker. Calbindin has been observed in 30% of myenteric neurons in immunohistochemical studies[16] while transcriptomic profiling finds more restricted expression[8]. Our analysis found Calb1Cre-tdT in <10% of myenteric neurons in all regions, and as low as 2% in the DC, agreeing with transcriptomic studies. Subsequent studies should investigate regional variation in combinatorial expression or neurochemical coding of neuronal clusters defined in scRNAseq studies, particularly for markers such as Penk or ChAT that are expressed in many different subtypes.

Our characterization of regional enteric organization and composition can serve as a blueprint to understand how local enteric neurocircuitry underlies region-specific motility patterns and function. Further, this anatomical map and computational approach can help inform our understanding of the pathophysiology of a wide range of diseases. Assessing ENS structure may help identify anatomical changes in human GI diseases with no known correlates within the ENS, such as intestinal pseudo-obstruction[43]. Additionally, neurodegenerative disorders such as Parkinson's disease and Alzheimer's disease have

identified ENS pathologies[44], yet the regional differences, spatial organization, and subtype identities of affected enteric neurons are unknown. Comprehensive analyses of CNS structure have served as platforms to dissect basic physiology and disease, and our work represents a parallel step toward an intricate understanding of the ENS.

STAR Methods

Resource availability

Lead contact—Further information and requests for resources and reagents should be directed to and will be fulfilled by the lead contact, Julia A. Kaltschmidt (jukalts@stanford.edu)

Materials availability—This study did not generate new unique reagents.

Data and code availability

- All data reported in this paper will be shared by the lead contact upon request.

- All original code has been deposited at Zenodo and is publicly available as of the date of publication. DOIs are listed in the key resources table.

- Any additional information required to reanalyze the data reported in this paper is available from the lead contact upon request.

Experimental model and subject details

Animals—All procedures conformed to the National Institutes of Health Guidelines for the Care and Use of Laboratory Animals and were approved by the Stanford University Administrative Panel on Laboratory Animal Care or the University of Chicago Institutional Animal Use and Care Committee. Mice were group housed up to a maximum of five adults per cage. Food and water were provided *ad libitum* and mice were maintained on a 12:12 LD cycle. For embryonic experiments, female mice were visually inspected for the presence of a vaginal plug every morning, and plugged females were separated from breeding cages.

X-ray tomography data was obtained from 13–15-week-old female C57BL/6J mice (Jackson, #000664). All experiments on the development of enteric neuronal organization were performed on C57BL/6J mice at the ages indicated. Experiments assessing neuronal subtype distribution used the marker lines detailed in the Key Resources table, from both sexes. Lines expressing Cre recombinase were crossed with Cre-dependent tdTomato (tdT). Investigations assessing general neuronal structure of the ENS collated data from all listed lines, from both sexes, aged 2–6 months.

Method details

Marker selection—For experiments assessing neuronal subtype distribution, we selected a variety of markers (via either genetically encoded reporters, or antibodies (Key Resources table)) covering calcium binding proteins, neurotransmitters and neuropeptides, which are known determinants of enteric subtype function or which delineate functionally relevant populations[7,8]. The markers included in the study were chosen based on several criteria:

(i) they have been shown to be relevant to enteric neurobiology, (ii) they cover markers previously used to identify functional neuronal subtypes (e.g. as in Qu et al.[7]), (iii) they delineate a limited number of clusters in recent RNAseq screens (such as VGLUT2 in ENC7 and ENC12, Sst in ENC5, Gad2 in ENC10 from Morarach et al.[8]) and (iv) it was possible to count them unambiguously (i.e. there was strong staining within the soma), either through immunostaining or available Cre recombinase lines, facilitating automated counting.

Calretinin, ChAT, and Tac1 are all known to mark excitatory motor neurons[1,15,45]. Penk also marks excitatory motor populations, in addition to some interneurons[1,15]. Somatostatin has been suggested to delineate a population of interneurons[17], as does myenteric 5-HT[46]. nNOS, VIP and PACAP have all been suggested to mediate inhibitory neuromuscular transmission[14,47]. Calbindin is suggested to mark sensory neurons[16]. The functions of VGLUT2 and Gad2 neurons are not known, but were included as they are well-known neurotransmitter markers in other areas of the nervous system and had been identified in the ENS by recent scRNAseq studies as belonging to specific subpopulations[8,41]. The same applies to tyrosine hydroxylase (TH), known to be expressed in intrinsic enteric neurons, though its function remains elusive[48,49]. Secretagogin, a CBP first identified in the pancreas[50,51], was similarly identified recently, and has not yet been described in the ENS.

Immunohistochemistry—For investigations into the structure of the adult ENS, the small intestine and colon were dissected out from 2–6 months-old mice culled by CO_2 and cervical dislocation. Intestines were flushed of fecal contents using cold PBS before cutting the proximal, middle and distal 2–3 cm of the small intestine to isolate the duodenum, jejunum and ileum. The colon was cut in two, and all segments were pinned to Sylgard 170 under light tension in cold PBS on ice. The mesentery was cut away, then each segment was cut open longitudinally along the mesenteric border. The tissue was then stretched flat and pinned to the Sylgard, muscularis facing upwards, and fixed in 4% PFA for 90 minutes at 4°C with shaking. For adult single-plexus wholemount preparations, the muscularis (both muscle layers and MP) was peeled away once fixed using fine forceps and a cotton bud.

For neonatal ages (postnatal days 0, 10, 15, and 21), intestines were cut open along the mesenteric border, pinned mucosa-down on Sylgard 170 in ice-cold PBS, and the muscularis was peeled away with fine forceps. Muscularis tissue was stored in ice-cold PBS and then pinned onto Sylgard 170 in a flat sheet in 35 mm glass dishes using insect pins. Tissue was immediately fixed as described above. Residual PFA was removed via PBS washes before proceeding directly to immunostaining, or tissue was stored in PBS containing 0.1% sodium azide for up to 3 weeks at 4°C.

For swiss roll section collection, the intestines were dissected as above. The SI was divided into duodenum, jejunum and ileum, while the colon was kept intact. A glass rod was placed through each segment and placed on filter paper. A scalpel was used to open each segment, and the glass rod was used to gently flatten the opened tissue so that the mucosa was facing up and the muscularis was flat against the filter paper. The tissue and filter paper were stacked on top of each other and placed in 4% PFA at 4°C for 90 minutes. Following 3 PBS washes, the stack was placed in 30% sucrose overnight for cryopreservation. The following day, each segment was rolled up into a spiral from distal to proximal and embedded in OCT

(Tissue-Tek) before being frozen on dry ice and stored at −80°C. To section, embedded tissue was allowed to equilibrate to −16°C in a cryostat (Leica CM3050 S), and 16 μm sections were collected on slides such that a single section contained the full length of a tissue segment.

For embryonic experiments, pregnant mice were culled by CO_2 and cervical dislocation. The uterus was removed, and embryos were placed in ice-cold PBS. The intestines were dissected from each embryo, and the mesentery was carefully removed. To measure intestinal length, the cleaned intestine was laid adjacent to a ruler. In a Sylgard 170 plate, a pin was placed in the stomach and anus to keep the intestines taut and straight. Tissue was fixed in 4% PFA for 90 minutes at 4°C with shaking.

For immunohistochemistry, large intact pieces of tissue were cut into smaller pieces (size dependent on the experiment and age, but typically ~7×7 mm^2) and transferred to WHO microtitration trays (International Scientific Supplies) containing PBS. Tissue was then put into PBT (PBS, 1% BSA, 0.1% Triton X-100) containing the primary antibodies overnight at 4°C with shaking. For mouse antibodies, tissue was pre-treated first with Affinipure FAb Fragment Donkey Anti-mouse (Jackson 715-007-003) diluted 1:50 in PBT, and then in 5% normal goat serum in PBT, for 2 h each prior to primary antibody incubation[8]. The following day, tissue was washed 3 times in PBT for 30 minutes each before transferring to PBT containing secondary antibodies for 2 h at room temperature with shaking. Tissue was washed twice in PBT and twice in PBS, then mounted onto slides using a paintbrush. Any folds or bumps in mounted tissue were removed by gentle manipulation with paint brushes under a dissection microscope. The tissue was allowed to partly air-dry, then was rinsed in ddH$_2$O and coverslipped using Fluoromount-G (Southern Biotech).

For embryonic experiments, immunohistochemistry was done as in adults with the following changes. Intact intestines were placed in WHO microtitration trays and treated as above. After immunohistochemistry, fixed intestines were cannulated with a cleaning wire for 33-gauge needles (Hamilton) and cut along the wire. Embryonic intestines were mounted full-thickness.

For swiss roll immunohistochemistry, sections on slides were stained as in adult wholemount tissue but staining was performed in a stationary incubation chamber to prevent drying out.

X-ray tomography—Mice were deeply anesthetized using pentobarbital (60 mg/kg intraperitoneal) to be non-responsive to toe pinch and transcardially perfused with 10 ml of 0.1 M sodium cacodylate buffer (Electron Microscopy Sciences (EMS)) to flush the vasculature followed by buffered fixative made of 2.5% glutaraldehyde (EMS), 2% paraformaldehyde (EMS) in 0.1 M sodium cacodylate buffer (EMS). The intestines were removed, and the mesentery was gently severed. The intestines were divided into segments (duodenum, jejunum, ileum, proximal and distal colon). Ileum and proximal colon were dissected out and gently flushed with 0.1 M sodium cacodylate buffer (EMS). The dissected segments were post-fixed overnight at 4°C in the fixative described above. After post-fixation, the intestines were cut open along the mesentery and dissected into

smaller pieces before staining with heavy metals as described by Hua et al[52]. Briefly, the tissues were extensively washed in 0.1 M sodium cacodylate buffer (EMS). This was followed by sequential staining with 2% buffered osmium tetroxide (EMS), 2.5% potassium ferrocyanide (Sigma-Aldrich) with no rinse in between followed by pyrogallol (Sigma-Aldrich), unbuffered 2% osmium tetroxide (EMS), 1% uranyl acetate (EMS), and 0.66% aspartic acid buffered lead (II) nitrate (Sigma-Aldrich) with extensive rinses in between each of the steps. The stained tissues were dehydrated in graded ethanol, propylene oxide and infiltrated with epon resin (EMS). The tissues were finally embedded in fresh epon and cured in an oven at 60°C for 48 h[52,53].

The epon embedded samples were imaged at 32-ID beamline at the Advanced Photon Source (APS) in Argonne National Laboratory. The sample was placed on a rotation stage and projection images were acquired at 600 nm/pixel resolution as the sample was rotated over 180 degrees[54,55]. The acquired images were 3D-reconstructed using the TomoPy toolbox[56].

Image acquisition—Images were acquired using a 20x (NA 0.75) oil objective on a Leica SP8 confocal microscope. Regions to be imaged were identified, acquired and stitched using the Navigator mode within LASX (Leica). A z-stack of the entire region was taken, ensuring that the full depth of the area of interest (e.g. the myenteric plexus) was captured in all tiles. Z-stacks were acquired with 3 μm between each focal plane for adult tissue and with 2 μm between each focal plane for embryonic and neonatal tissue.

Quantification and statistical analysis

X-ray tomography analysis—3D-reconstructed data were manually annotated using Knossos, an open-source software (https://knossos.app/)[57]. We identified the myenteric ganglia in between the circular and longitudinal muscle layers and the submucosal ganglia in the submucosal space. All cell bodies were identified based on the circular outline and the presence of a nucleus within the cell.

Image Analysis

Cell counting: Image analysis was primarily performed using ImageJ/FIJI (NIH, Bethesda, MD). For neuronal density analysis, HuC/D images (maximum intensity projections for adults, single plane for embryonic/neonatal) were blurred before thresholding and watershedding. Cells were counted using the Analyze Particles function, and density was calculated based on area of tissue measured in FIJI. To count neuronal subtypes, the Image Calculator function was used to combine thresholded HuC/D stacks (prior to maximum projection) with raw image stacks of a defined cell type. The result of this calculation was then maximally projected and counted in an automated fashion as described above. The exceptions to this were 5-HT and TH, which were counted manually after being combined with the thresholded HuC/D image stack, and were identified by their distinctive cytoplasmic expression pattern. To quantify apoptotic neurons in the embryonic/neonatal intestines, the Image Calculator function was used to combine thresholded HuC/D maximum projections with raw maximum projections of Caspase-3 labeling. The result was then counted as above.

Conditional intensity function (CIF) analysis: To visualize and evaluate spatial patterns, we calculated the conditional intensity function (CIF), which generates a spatial density map of neuron locations relative to a given neuron. Square images measuring ~1800×1800 μm for adult and ~400×400 μm for embryonic and neonatal tissue, respectively, were processed in FIJI as described above, and the XY coordinates of each neuron were obtained using Analyze Particles. We empirically estimated the CIF for a given sample by iterating over all neurons and calculating the number of neurons in a 2D grid around that neuron. Total image area was normalized to 1, divided into 100 bins per unit length. The 2D grid's width and height were both 0.7 for adult data, while they were 0.8 and 0.5, respectively, for embryonic/neonatal data. Density values were normalized to expected density based on a uniform distribution of neurons, given a value of 1. We excluded the center grid point from the resulting CIF plot, which included data from the neuron used for conditioning.

We then transformed the 2D grid into a one-dimensional line by averaging along the y-axis, using either the full y-axis (for interstripe distance calculations) or a smaller proportion (for stripe width calculations). For adult data, this smaller proportion was a length of 0.1 relative image length above and below the center, and for developmental data, we used a value of 0.2. For developmental data, which contained far fewer neurons, we smoothed with a Gaussian of 20 μm standard deviation. We then identified the first minima and first peak next to the center. Stripe width was taken as the width at the half height from minimum to center peak. Interstripe distance was taken as the distance between the left and center peaks. For interstripe distance analysis, samples in which secondary stripes could not be unambiguously identified were not included. All analyses were implemented in Python.

Nearest-neighbor and Empirical distribution function (EDF) analysis: To assess enteric neuron organization across development, we tested each of the samples for deviation from a hypothesis of random neuron positions, known as complete spatial randomness. Our analysis was based on nearest-neighbor distances. The distribution of nearest-neighbor distances under complete spatial randomness can be calculated[58]. Specifically, the mean of the distribution and its variance can be approximated by a normal distribution[58]. Embryonic and neonatal images were processed as above to generate XY coordinates, and then for each sample we calculated the mean of the data and extracted a z-score for the deviation of the data from the expected value. In addition, to better visualize deviations, we generated synthetic samples under the assumption of complete spatial randomness. We then plotted the empirical distribution function for the data as well as an envelope defined by the maximum and minimum of the empirical distribution function over 500 synthetic samples.

We observed that some deviation from randomness was driven mostly by the fact that the synthetically generated samples exhibited overlap in space while our data, taken from a single-plane image, did not overlap. To make the analysis more robust to this property, we generated synthetic samples with a minimum distance imposed. We chose this minimum distance as 10 μm, approximately the average diameter of an enteric neuron across all ages examined. We then generated 500 random samples and calculated their z-score and defined a metric that is the difference between the z-score of the data and the mean of the z-score of the synthetic samples. This allowed better identification of differences from other spatial properties (e.g., stripes). All analyses were implemented in Python.

Longitudinal axis signal profile analysis: Profiles of HuC/D and neuronal subtype signal intensity along the longitudinal tissue axis were generated in FIJI using the Plot Profile function, once the image had been adequately aligned such that the longitudinal axis of the tissue matched the x-axis. These profiles were then exported to Prism 9 (GraphPad) for correlation analysis (see Statistical analysis). After analysis, profiles were smoothed in Prism 9 by averaging 12.5 μm either side of a given point to aid in visualizing peaks in intensity. To calculate the number of HuC/D neurons and neurons of a given subtype present in stripes within an image, smoothed profiles were first exported to Microsoft Excel and peaks in the data were automatically identified. The locations of these peaks were then exported to FIJI, which created a box measuring the full y-axis and 50 μm either side of each peak location. This box would constitute a stripe, and Analyze Particles was used on thresholded images (as above) to count the number of objects within each stripe. This data was converted to frequency distributions in Prism 9.

General statistical analysis—Statistical tests and graphical representation of data were performed using Prism 9 software (GraphPad). Statistical comparisons were performed using one-way ANOVA to assess if age or intestinal region were significant factors for a variety of measurements (neuronal density, intestine length, etc.); repeated measures one-way ANOVAs were used for intestinal region. Mixed effects models were used in cases of missing data. Tukey's or Dunnett's correction for multiple comparisons were used where appropriate to determine significant differences ($p<0.05$) between individual regions or ages. The results of these corrections are indicated on graphs as letters to indicate significant differences. Two-way ANOVAs were used to determine the effect of sex on neuronal cytoarchitecture, followed by Šídák's multiple comparisons tests. Correlation was determined using Pearson's correlation coefficient. The Kolmogorov-Smirnov (KS) test was used to compare the frequency distributions of neuron subtypes as a proportion of neurons in neuronal stripes. Full details of these statistical tests can be found in Table S1.

Supplementary Material

Refer to Web version on PubMed Central for supplementary material.

Acknowledgements

References

1. Furness JB (2012). The enteric nervous system and neurogastroenterology. Nat. Rev. Gastroenterol. Hepatol 9, 286–294. [PubMed: 22392290]

2. Irwin D (1931). The anatomy of Auerbach's plexus. Am. J. Anat 49, 141–166.

3. Lei J, and Howard MJ (2011). Targeted deletion of Hand2 in enteric neural precursor cells affects its functions in neurogenesis, neurotransmitter specification and gangliogenesis, causing functional aganglionosis. Development 138, 4789–4800. [PubMed: 21989918]

4. Breau MA, Pietri T, Eder O, Blanche M, Brakebusch C, Fässler R, Thiery JP, and Dufour S (2006). Lack of β1 integrins in enteric neural crest cells leads to a Hirschsprung-like phenotype. Development 133, 1725–1734. [PubMed: 16571628]

5. Li Z, Hao MM, Van Den Haute C, Baekelandt V, Boesmans W, and Berghe P. Vanden (2019). Regional complexity in enteric neuron wiring reflects diversity of motility patterns in the mouse large intestine. Elife 8, 1–27.

6. Sasselli V, Boesmans W, Berghe P. Vanden, Tissir F, Goffinet AM, and Pachnis V (2013). Planar cell polarity genes control the connectivity of enteric neurons. J. Clin. Invest 123, 1763–1772. [PubMed: 23478408]

7. Qu ZD, Thacker M, Castelucci P, Bagyánszki M, Epstein ML, and Furness JB (2008). Immunohistochemical analysis of neuron types in the mouse small intestine. Cell Tissue Res. 334, 147–161. [PubMed: 18855018]

8. Morarach K, Mikhailova A, Knoflach V, Memic F, Kumar R, Li W, Ernfors P, and Marklund U (2021). Diversification of molecularly defined myenteric neuron classes revealed by single-cell RNA sequencing. Nat. Neurosci 24, 34–46. [PubMed: 33288908]

9. Drokhlyansky E, Smillie CS, Wittenberghe N. Van, Ericsson M, Griffin GK, Eraslan G, Dionne D, Cuoco MS, Goder-Reiser MN, Sharova T, et al. (2020). The Human and Mouse Enteric Nervous System at Single-Cell Resolution. Cell 182, 1–17. [PubMed: 32649872]

10. Burns AJ, Roberts RR, Bornstein JC, and Young HM (2009). Development of the enteric nervous system and its role in intestinal motility during fetal and early postnatal stages. Semin. Pediatr. Surg 18, 196–205. [PubMed: 19782301]

11. Fung C, and Vanden Berghe P (2020). Functional circuits and signal processing in the enteric nervous system. Cell. Mol. Life Sci 77, 4505–4522. [PubMed: 32424438]

12. Rao M, and Gershon MD (2016). The bowel and beyond: The enteric nervous system in neurological disorders. Nat. Rev. Gastroenterol. Hepatol 13, 517–528. [PubMed: 27435372]

13. Spencer NJ, and Hu H (2020). Enteric nervous system: sensory transduction, neural circuits and gastrointestinal motility. Nat. Rev. Gastroenterol. Hepatol 2020 17, 338–351.

14. Costa M, Furness JB, Pompolo S, Brookes SJH, Bornstein JC, Bredt DS, and Snyder SH (1992). Projections and chemical coding of neurons with immunoreactivity for nitric oxide synthase in the guinea-pig small intestine. Neurosci. Lett 148, 121–125. [PubMed: 1284439]

15. Brookes SJH, Steele PA, and Costa M (1991). Calretinin immunoreactivity in cholinergic motor neurones, interneurones and vasomotor neurones in the guinea-pig small intestine. Cell Tissue Res. 263, 471–481. [PubMed: 1715238]

16. Furness JB, Trussell DC, Pompolo S, Bornstein JC, and Smith TK (1990). Calbindin neurons of the guinea-pig small intestine: quantitative analysis of their numbers and projections. Cell Tissue Res. 260, 261–272. [PubMed: 2357722]

17. Portbury AL, Pompolo S, Furness JB, Stebbing MJ, Kunze WAA, Bornstein JC, and Hughes S (1995). Cholinergic, somatostatin-immunoreactive interneurons in the guinea pig intestine: Morphology, ultrastructure, connections and projections. J. Anat 187, 303–321. [PubMed: 7591994]

18. Lasrado R, Boesmans W, Kleinjung J, Pin C, Bell D, Bhaw L, McCallum S, Zong H, Luo L, Clevers H, et al. (2017). Lineage-dependent spatial and functional organization of the mammalian enteric nervous system. Science. 356, 722–726. [PubMed: 28522527]

19. Bornstein JC, Furness JB, Smith TK, and Trussell DC (1991). Synaptic responses evoked by mechanical stimulation of the mucosa in morphologically characterized myenteric neurons of the guinea-pig ileum. J. Neurosci 11, 505–518. [PubMed: 1846909]

20. Le Douarin NM, and Teillet MA (1973). The migration of neural crest cells to the wall of the digestive tract in avian embryo. J. Embryol. Exp. Morphol 30, 31–48. [PubMed: 4729950]

21. Anderson RB, Stewart AL, and Young HM (2006). Phenotypes of neural-crest-derived cells in vagal and sacral pathways. Cell Tissue Res. 323, 11–25. [PubMed: 16133146]

22. Wang X, Chan AKK, Sham MH, Burns AJ, and Chan WY (2011). Analysis of the sacral neural crest cell contribution to the hindgut enteric nervous system in the mouse embryo. Gastroenterology 141, 992–1002.e6. [PubMed: 21699792]

23. Barlow AJ, Wallace AS, Thapar N, and Burns AJ (2008). Critical numbers of neural crest cells are required in the pathways from the neural tube to the foregut to ensure complete enteric nervous system formation. Development 135, 1681–1691. [PubMed: 18385256]

24. Wallace AS, Barlow AJ, Navaratne L, Delalande JM, Tauszig-Delamasure S, Corset V, Thapar N, and Burns AJ (2009). Inhibition of cell death results in hyperganglionosis: Implications for enteric nervous system development. Neurogastroenterol. Motil 21, 768–778. [PubMed: 19400926]

25. Delalande JM, Natarajan D, Vernay B, Finlay M, Ruhrberg C, Thapar N, and Burns AJ (2014). Vascularisation is not necessary for gut colonisation by enteric neural crest cells. Dev. Biol 385, 220–229. [PubMed: 24262984]

26. Nestor-Kalinoski A, Smith-Edwards KM, Meerschaert K, Margiotta JF, Rajwa B, Davis BM, and Howard MJ (2022). Unique Neural Circuit Connectivity of Mouse Proximal, Middle, and Distal Colon Defines Regional Colonic Motor Patterns. Cell. Mol. Gastroenterol. Hepatol 13, 309–337.e3. [PubMed: 34509687]

27. Chevalier NR, Agbesi RJA, Ammouche Y, and Dufour S (2021). How Smooth Muscle Contractions Shape the Developing Enteric Nervous System. Front. Cell Dev. Biol 9, 678975. [PubMed: 34150774]

28. Huycke TR, Miller BM, Gill HK, Nerurkar NL, Sprinzak D, Mahadevan L, and Tabin CJ (2019). Genetic and Mechanical Regulation of Intestinal Smooth Muscle Development. Cell 179, 90–105.e21. [PubMed: 31539501]

29. Chevalier NR, Ammouche Y, Gomis A, Langlois L, Guilbert T, Bourdoncle P, and Dufour S (2021). A neural crest cell isotropic-to-nematic phase transition in the developing mammalian gut. Commun. Biol 4, 770. [PubMed: 34162999]

30. Schlieve CR, Fowler KL, Thornton M, Huang S, Hajjali I, Hou X, Grubbs B, Spence JR, and Grikscheit TC (2017). Neural Crest Cell Implantation Restores Enteric Nervous System Function and Alters the Gastrointestinal Transcriptome in Human Tissue-Engineered Small Intestine. Stem Cell Reports 9, 883–896. [PubMed: 28803915]

31. Workman MJ, Mahe MM, Trisno S, Poling HM, Watson CL, Sundaram N, Chang CF, Schiesser J, Aubert P, Stanley EG, et al. (2017). Engineered human pluripotent-stem-cell-derived intestinal tissues with a functional enteric nervous system. Nat. Med 23, 49–59. [PubMed: 27869805]

32. May-Zhang AA, Tycksen E, Southard-Smith AN, Deal KK, Benthal JT, Buehler DP, Adam M, Simmons AJ, Monaghan JR, Matlock BK, et al. (2021). Combinatorial Transcriptional Profiling of Mouse and Human Enteric Neurons Identifies Shared and Disparate Subtypes In Situ. Gastroenterology 160, 755–770.e26. [PubMed: 33010250]

33. Goldstein N, McKnight AD, Carty JRE, Arnold M, Betley JN, and Alhadeff AL (2021). Hypothalamic detection of macronutrients via multiple gut-brain pathways. Cell Metab. 33, 676–687.e5. [PubMed: 33450178]

34. Obata Y, Castaño Á, Boeing S, Bon-Frauches AC, Fung C, Fallesen T, de Agüero MG, Yilmaz B, Lopes R, Huseynova A, et al. (2020). Neuronal programming by microbiota regulates intestinal physiology. Nature 578, 284–289. [PubMed: 32025031]

35. Muller PA, Schneeberger M, Matheis F, Wang P, Kerner Z, Ilanges A, Pellegrino K, Mármol J, Castro TBR, Furuichi M, et al. (2020). Microbiota modulate sympathetic neurons via a gut – brain circuit. Nature 583, 441–446. [PubMed: 32641826]

36. Smith-Edwards KM, Edwards BS, Wright CM, Schneider S, Meerschaert KA, Ejoh LL, Najjar SA, Howard MJ, Albers KM, Heuckeroth RO, et al. (2021). Sympathetic Input to Multiple Cell Types in Mouse and Human Colon Produces Region-Specific Responses. Gastroenterology 160, 1208–1223.e4. [PubMed: 32980343]

37. Brookes SJH (2001). Classes of enteric nerve cells in the guinea-pig small intestine. Anat. Rec 262, 58–70. [PubMed: 11146429]

38. Muller PA, Matheis F, Schneeberger M, Kerner Z, Jové V, and Mucida D (2020). Microbiota-modulated CART enteric neurons autonomously regulate blood glucose. Science. 6176, 314–321.

39. Matheis F, Muller PA, Graves CL, Gabanyi I, Kerner ZJ, Costa-Borges D, Ahrends T, Rosenstiel P, and Mucida D (2020). Adrenergic Signaling in Muscularis Macrophages Limits Infection-Induced Neuronal Loss. Cell 180, 64–78.e16. [PubMed: 31923400]

40. Erickson CS, Lee SJ, Barlow-Anacker AJ, Druckenbrod NR, Epstein ML, and Gosain A (2014). Appearance of cholinergic myenteric neurons during enteric nervous system development: Comparison of different ChAT fluorescent mouse reporter lines. Neurogastroenterol. Motil 26, 874–884. [PubMed: 24712519]

41. Zeisel A, Hochgerner H, Lönnerberg P, Johnsson A, Memic F, van der Zwan J, Häring M, Braun E, Borm LE, La Manno G, et al. (2018). Molecular Architecture of the Mouse Nervous System. Cell 174, 999–1014. [PubMed: 30096314]

42. Furness JB, Costa M, and Miller RJ (1983). Distribution and projections of nerves with enkephalin-like immunoreactivity in the guinea-pig small intestine. Neuroscience 8, 653–664. [PubMed: 6306502]

43. Melo dos Santos AL, Wander Almeida Braga R, Bender Kohnert Seidler H, Pinheiro de Abreu Miranda R, Itália Teixeira Salvador I, and de Carvalho E (2020). Pediatric intestinal pseudo-obstruction: Role of histopathology. J. Pediatr. Surg. Case Reports 57, 101449.

44. Chalazonitis A, and Rao M (2018). Enteric nervous system manifestations of neurodegenerative disease. Brain Res. 1693, 207–213. [PubMed: 29360466]

45. Brookes SJH, Steele PA, and Costa M (1991). Identification and immunohistochemistry of cholinergic and non-cholinergic circular muscle motor neurons in the guinea-pig small intestine. Neuroscience 42, 863–878. [PubMed: 1720229]

46. Monro RL, Bertrand PP, and Bornstein JC (2002). ATP and 5-HT are the principal neurotransmitters in the descending excitatory reflex pathway of the guinea-pig ileum. Neurogastroenterol. Motil 14, 255–264. [PubMed: 12061910]

47. Lecci A, Santicioli P, and Maggi CA (2002). Pharmacology of transmission to gastrointestinal muscle. Curr. Opin. Pharmacol 2, 630–641. [PubMed: 12482724]

48. Li ZS, Pham TD, Tamir H, Chen JJ, and Gershon MD (2004). Enteric Dopaminergic Neurons: Definition, Developmental Lineage, and Effects of Extrinsic Denervation. J. Neurosci 24, 1330–1339. [PubMed: 14960604]

49. Neuhuber W, and Wörl J (2018). Monoamines in the enteric nervous system. Histochem. Cell Biol 150, 703–709. [PubMed: 30250972]

50. Maj M, Wagner L, and Tretter V (2019). 20 Years of Secretagogin: Exocytosis and Beyond. Front. Mol. Neurosci 12, 29. [PubMed: 30853888]

51. Wagner L, Oliyarnyk O, Gartner W, Nowotny P, Groeger M, Kaserer K, Waldhausl W, and Pasternack MS (2000). Cloning and expression of secretagogin, a novel neuroendocrine- and pancreatic islet of Langerhans-specific Ca2+-binding protein. J. Biol. Chem 275, 24740–24751. [PubMed: 10811645]

52. Hua Y, Laserstein P, and Helmstaedter M (2015). Large-volume en-bloc staining for electron microscopy-based connectomics. Nat. Commun 6, 7923. [PubMed: 26235643]

53. Tapia JC, Kasthuri N, Hayworth KJ, Schalek R, Lichtman JW, Smith SJ, and Buchanan J (2012). High-contrast en bloc staining of neuronal tissue for field emission scanning electron microscopy. Nat. Protoc 7, 193–206. [PubMed: 22240582]

54. Dyer EL, Roncal WG, Prasad JA, Fernandes HL, Gürsoy D, De Andrade V, Fezzaa K, Xiao X, Vogelstein JT, Jacobsen C, et al. (2017). Quantifying mesoscale neuroanatomy using X-ray microtomography. eNeuro 4, 1–18.

55. Prasad JA, Balwani AH, Johnson EC, Miano JD, Sampathkumar V, De Andrade V, Fezzaa K, Du M, Vescovi R, Jacobsen C, et al. (2020). A three-dimensional thalamocortical dataset for characterizing brain heterogeneity. Sci. Data 7, 358. [PubMed: 33082340]

56. Gürsoy D, De Carlo F, Xiao X, and Jacobsen C (2014). TomoPy: A framework for the analysis of synchrotron tomographic data. J. Synchrotron Radiat 21, 1188–1193. [PubMed: 25178011]

57. Boergens KM, Berning M, Bocklisch T, Bräunlein D, Drawitsch F, Frohnhofen J, Herold T, Otto P, Rzepka N, Werkmeister T, et al. (2017). WebKnossos: Efficient online 3D data annotation for connectomics. Nat. Methods 14, 691–694. [PubMed: 28604722]

58. Diggle PJ (2013). Statistical analysis of spatial and spatio-temporal point patterns 3rd ed. (Chapman and Hall/CRC).

59. Skarlatou S, Hérent C, Toscano E, Mendes CS, Bouvier J, and Zampieri N (2020). Afadin Signaling at the Spinal Neuroepithelium Regulates Central Canal Formation and Gait Selection. Cell Rep. 31.

60. Betley JN, Wright CVE, Kawaguchi Y, Erdélyi F, Szabó G, Jessell TM, and Kaltschmidt JA (2009). Stringent Specificity in the Construction of a GABAergic Presynaptic Inhibitory Circuit. Cell 139, 161–174. [PubMed: 19804761]

61. King PH, Redden D, Palmgren JS, Nabors LB, and Lennon VA (1999). Hu antigen specificities of ANNA-I autoantibodies in paraneoplastic neurological disease. J. Autoimmun 13, 435–443. [PubMed: 10585760]

62. Schindelin J, Arganda-Carreras I, Frise E, Kaynig V, Longair M, Pietzsch T, Preibisch S, Rueden C, Saalfeld S, Schmid B, et al. (2012). Fiji: an open-source platform for biological-image analysis. Nat. Methods 9, 676–82. [PubMed: 22743772]

Highlights

- Myenteric neurons, but not submucosal neurons, form circumferential stripes.

- Conditional intensity function plots quantify and reveal tissue organization.

- Neuronal stripes arise from proximal-to-distal during embryonic development.

- Neuronal marker expression differs by region but not among individual stripes.
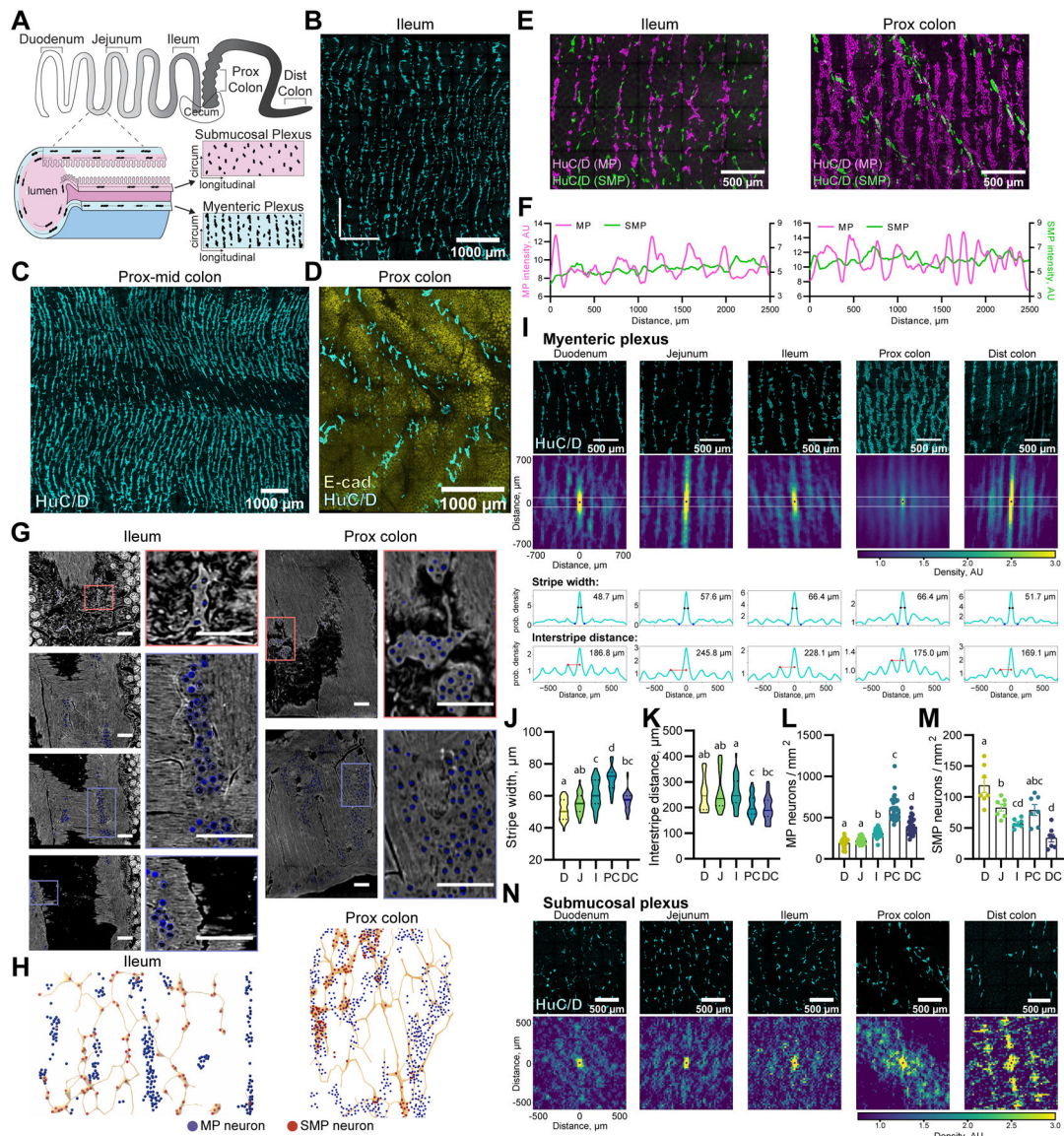
Figure 1 |. Regional organization of enteric neurons in the adult ENS.
(**A**) Schematic illustrating the regions of the intestines (top) and the structure and orientation of the submucosal (SMP) and myenteric plexuses (MP) within the intestine wall (bottom). Black ovals represent neurons. (**B-D**) Representative immunohistochemistry (IHC) images of adult wholemount MP of ileum (**B**) and proximal-mid colon (**C**) for neuronal label HuC/D, and SMP of PC (**D**) for HuC/D (cyan) and epithelial label E-cadherin (yellow). (**E**) Representative images of immunohistochemical staining of full-thickness wholemount tissue of ileum (left) and PC (right) for HuC/D (MP: magenta, SMP: green). (**F**) Smoothed profiles of HuC/D signal intensity along the longitudinal (x-)axis of images in (**E**), highlighting stripes (peaks) in MP (magenta) and lack thereof in SMP (green). (**G**) Representative X-ray tomography images of heavy metal staining of adult ileum (left) and PC (right). Colored boxes represent locations of magnified images. Cell bodies identified based on morphology and location, annotated with blue circles. (**H**) Schematic of MP (blue) and SMP (red) cell

body locations from samples in (**G**). Yellow shading represents the SMP. (**I**) Organizational analysis of wholemount MP HuC/D IHC of all intestinal regions (top) using conditional intensity functions (CIFs; 2nd row), showing probability density of neuron locations. A value of 1 is expected density based on uniform neuron distribution. CIFs: yellow: high probability density; blue: low. Axes apply to all panels. CIFs collapsed onto 2D plot to calculate 50% stripe width (3rd row, analysis of region within white lines on CIF, black dots: width measurement, blue dots: trough) and interstripe distance (bottom, includes full CIF plot, distance calculated between red dots). Inset values show given stripe width and interstripe distance values for representative samples. (**J,K**) Violin plots of stripe width (**J**) and interstripe distance (**K**) from MP wholemount preparations analyzed by CIFs as in (**I**). n = 34 mice for all groups (**J**) and n = 21–29 (**K**). (**L,M**) Neuronal density (mean ± SEM) in MP (**L**) and SMP (**M**) across intestinal regions. n = 34 (**L**) and 7 (**M**). (**N**) Organizational analysis of wholemount SMP HuC/D IHC of all intestinal regions (top) using CIFs (2nd row) as in (**I**). Lack of obvious stripe structure precluded further analysis. All tests one-way ANOVA, other than (**K**) which used a mixed-effects model. Letters represent significant differences, such that two groups are not significantly different if they share a common letter. Full details of pairwise comparisons can be found in Table S1. Scale bars as indicated. AU, arbitrary units; D, duodenum; DC, distal colon; I, ileum; J, jejunum; PC, proximal colon. See also Figure S1.

Figure 2 |. Progressive organization of the developing MP.

(**A**) Representative images of immunohistochemical staining with neuronal marker HuC/D in intestinal wholemount preparations from the jejunum and DC MP over developmental time. Images are a subset of those in Figure S1A. (**B**) CIF plots of wholemount MP HuC/D IHC in the jejunum and DC over developmental time. Yellow: high probability density; blue: low. Axes apply to all panels. (**C**) 2D arrays of neurons (HuC/D) and corresponding synthetically generated pseudorandom data for embryonic day (E)16.5 and postnatal day (P)10 DC. Empirical distribution function (EDF) plots for neurons (blue line) and synthetically generated maximum and minimum (gray lines). Inset values indicate z-score difference between data and mean of synthetic values for a representative sample. (**D**) z-score difference between data and mean of synthetically generated values (mean ± SEM) derived from EDF plots in all regions of the intestines over developmental time. n = 3–11. (**E,F**) Lengths of small intestine (**E**) and colon (**F**) (mean ± SEM). n = 3–15. (**G,H**) Neuronal density (mean ± SEM) in the jejunum (**G**) and DC (**H**). n = 3–11. (**I,J**) Violin plots of interstripe distance in the jejunum (**I**) and DC (**J**) as analyzed by CIFs, n = 3–11. (**K,L**) Representative images (**K**) and quantification (**L**; mean ± SEM) of immunohistochemical staining with HuC/D (magenta) and apoptotic marker Caspase-3 (green) in wholemount preparations of the MP from small intestine (top) and colon (bottom). n = 3–4. All tests

one-way ANOVA. Full details of pairwise comparisons can be found in Table S1. Scale bars as indicated. See also Figure S2.
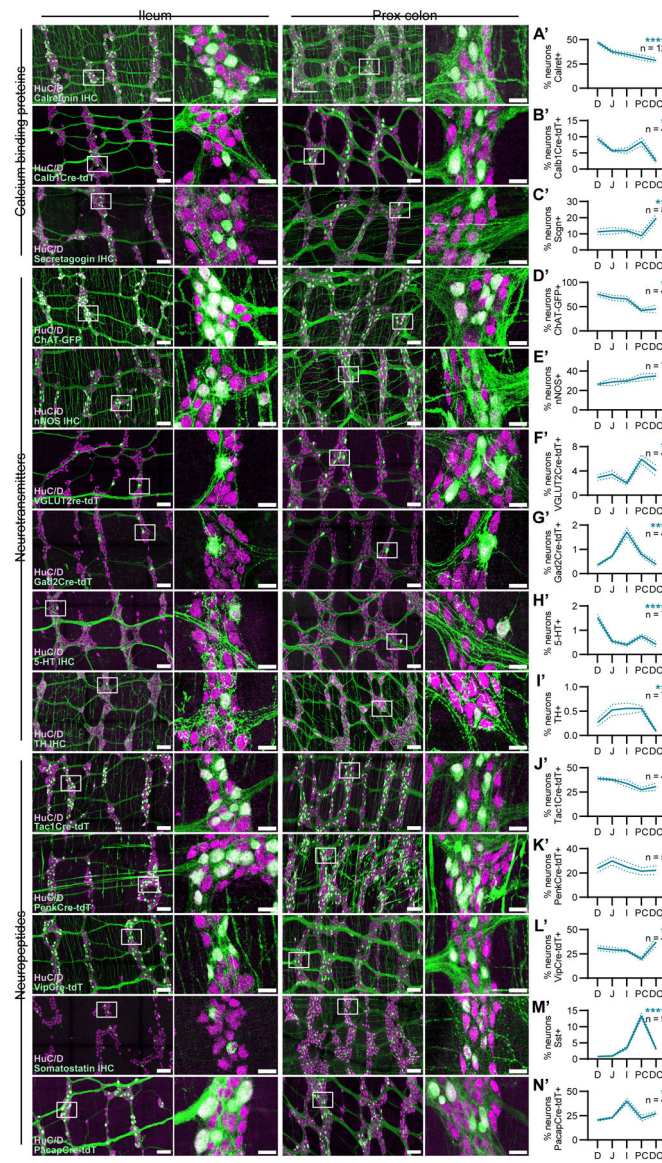
Figure 3 |. Regional distribution and organization of neuronal subtypes.
(**A-N**) Representative images of adult wholemount MPs showing immunohistochemical labels or genetically encoded reporters for calcium binding proteins (green, **A-C**), neurotransmitters (green, **D-I**) and neuropeptides (green, **J-M**) alongside neuronal label HuC/D (magenta) in the ileum (left) and PC (right). Higher magnification image locations indicated by white boxes. Scale bars 100 μm for full images, 25 μm for zoom ins. (**A'-N'**) Proportion of total HuC/D neurons (mean ± SEM) positive for each neuronal marker across intestinal regions as in (**A-N**). n as indicated in graphs. All tests one-way ANOVA. Full details of pairwise comparisons can be found in Table S1. *$p<0.05$, **$p<0.01$, ***$p<0.001$, ****$p<0.0001$. See also Figures S3,S4.
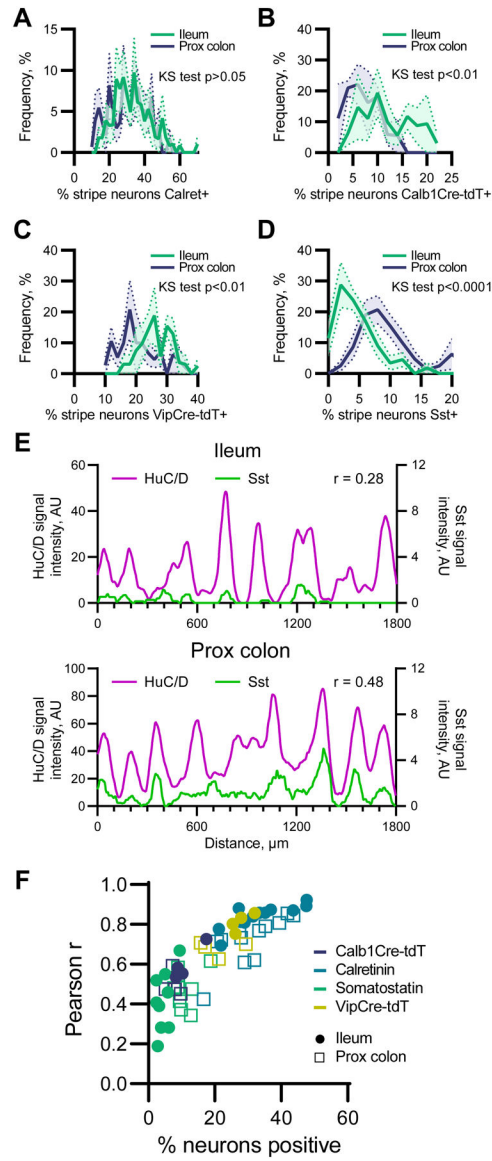
Figure 4 |. Structural distribution of neuronal subtypes.
(**A-D**) Frequency distribution plots (mean ± SEM) of the proportion of neurons in a neuronal stripe positive for calretinin (**A;** 7–12 stripes per region, 12 mice), Calb1Cre-tdT (**B;** 7–10 stripes, 4 mice), VipCre-tdT (**C;** 7–12 stripes, 4 mice) and somatostatin (**D;** 6–12 stripes, 9 mice). KS, Kolmogorov-Smirnov. (**E**) Representative smoothed profiles of HuC/D and somatostatin signal intensity along the longitudinal axis in ileum (top) and PC (bottom). r value indicates Pearson r correlation between the two profiles. (**F**) Scatter plot showing the relationship between the proportion of total (HuC/D) neurons positive for a given marker (Calb1Cre-tdT, calretinin, somatostatin or VipCre-tdT) in the ileum or PC and the Pearson r value for that sample, representing the strength of correlation between the HuC/D signal intensity profile and that of the marker (as in **E**). Note that the association is weaker

for lowly expressed markers (e.g. somatostatin) but rises steeply when more than ~5% of neurons are positive for a given marker. See also Figure S4.

Key resources table

REAGENT or RESOURCE	SOURCE	IDENTIFIER
Antibodies		
Mouse anti-Calbindin, 1:100	Swant	Cat# CB300 ; RRID: AB_10000347
Rabbit anti-Calretinin, 1:200	Millipore	Cat# AB5054; RRID: AB_2068506
Rabbit anti-Caspase3, 1:500	Abcam	Cat# AB2302; RRID: AB_302962
Rabbit anti-Choline acetyltransferase (ChAT) , 1:4000	Gift from Thomas Jessell/Susan Morton	Cat# CU1574[59]; RRID: AB_2750952
Rat anti-E-cadherin, 1:2000	ThermoFisher	Cat# 13-1900; RRID: AB_2533005
Rabbit anti-GAD65, 1:50000	Gift from Thomas Jessell/Susan Morton	Cat# CU1196[60] ; RRID: AB_2904512
Sheep anti-GFP, 1:1000	Biogenesis	Cat# 4745-1051; RRID: AB_619712
Human anti-HuC/D, 1:75000	Gift from Vanda Lennon	Cat# HuC/D_Lennon[61]; RRID: AB_2813895
Rabbit anti-met-Enkephalin, 1:1000	Immunostar	Cat# 20065; RRID: AB_572250
Sheep anti-nNOS, 1:1000	Millipore	Cat# AB1529; RRID: AB_90743
Rabbit anti-nNOS, 1:2000	Sigma-Aldrich	Cat# N7280; RRID: AB_260796
Chicken anti-Secretagogin, 1:3000	EnCor Bio	Cat# CPCA-SCGN; RRID: AB_2744521
Goat anti-Serotonin (5-HT) , 1:2000	Immunostar	Cat# 20079; RRID: AB_572262
Rat anti-Somatostatin, 1:500	Millipore	Cat# MAB354; RRID: AB_2255365
Rabbit anti-Substance P, 1:4000	Immunostar	Cat# 20064; RRID: AB_572266
Rabbit anti-Tyrosine hydroxylase (TH) , 1:2000	Pel-Freez	Cat# P40101-150 ; RRID: AB_2617184
Mouse anti-Tuj1, 1:2000	Sigma	Cat# T8578; RRID: AB_1841228
Guinea pig anti-VGLUT2, 1:3000	Synaptic Systems	Cat# 135 404; RRID: AB_887884
Donkey anti-Chicken Cy3	Jackson ImmunoResearch	Cat#703-165-155; RRID: AB_2340363
Donkey anti-Chicken AF 647	Jackson ImmunoResearch	Cat#703-605-155; RRID: AB_2340379
Donkey anti-Guinea pig AF 647	Jackson ImmunoResearch	Cat#706-605-148; RRID: AB_2340476
Donkey anti-Goat Cy3	Jackson ImmunoResearch	Cat#705-165-147; RRID: AB_2307351
Donkey anti-Goat AF 647	Jackson ImmunoResearch	Cat#705-605-003; RRID: AB_2340436
Donkey anti-Human AF 488	Jackson ImmunoResearch	Cat#709-545-149; RRID: AB_2340566
Donkey anti-Human AF 405	Jackson ImmunoResearch	Cat#709-475-149; RRID: AB_2340553
Donkey anti-Human AF 647	Jackson ImmunoResearch	Cat#709-605-149; RRID: AB_2340578
Goat anti-Mouse Cy3	Jackson ImmunoResearch	Cat#115-165-205; RRID: AB_2338694
Goat anti-Mouse AF 647	Jackson ImmunoResearch	Cat#115-605-205; RRID: AB_2338916

REAGENT or RESOURCE	SOURCE	IDENTIFIER
Donkey anti-Rabbit AF 488	Invitrogen	Cat#A21206; RRID: AB_2535792
Donkey anti-Rabbit Cy3	Jackson ImmunoResearch	Cat#711-165-152; RRID: AB_2307443
Donkey anti-Rabbit Cy5	Jackson ImmunoResearch	Cat#711-175-152; RRID: AB_2340607
Donkey anti-Rat AF 488	Invitrogen	Cat#A21208; RRID: AB_141709
Donkey anti-Rat Cy3	Jackson ImmunoResearch	Cat#712-165-153; RRID: AB_2340667
Donkey anti-Sheep AF 488	Invitrogen	Cat#A11015; RRID: AB_141362
Donkey anti-Sheep Cy5	Jackson ImmunoResearch	Cat#713-175-147; RRID: AB_2340730
FAb Fragment Donkey Anti-mouse	Jackson ImmunoResearch	Cat#715-007-003
Chemicals, peptides, and recombinant proteins		
Sodium Cacodylate Buffer, 0.2M, pH 7.4	Electron Microscopy Sciences	Cat#11653
Osmium tetroxide, 4% aqueous solution	Electron Microscopy Sciences	Cat#19190
Potassium hexacyanoferrate(II) trihydrate	Sigma-Aldrich	Cat#P3289
Pyrogallol	Sigma-Aldrich	Cat#P0381
4% Uranyl Acetate Solution	Electron Microscopy Sciences	Cat#22400-4
Lead(II) Nitrate	Sigma-Aldrich	Cat#228621
L-Aspartic acid	Sigma-Aldrich	Cat#A8949
Propylene oxide, EM grade	Electron Microscopy Sciences	Cat#20401
Embed-812 kit	Electron Microscopy Sciences	Cat#14120
Experimental models: Organisms/strains		
Mouse: C57BL/6J	The Jackson Laboratory	RRID: IMSR_JAX:000664
Mouse: ChAT-GFP; B6.Cg-Tg(RP23-268L19-EGFP)2Mik/J	The Jackson Laboratory	RRID: IMSR_JAX:007902
Mouse: Plp1-GFP; B6;CBA-Tg(Plp1-EGFP)10Wmac/J	The Jackson Laboratory	RRID: IMSR_JAX:033357
Mouse: Calb1Cre; B6;129S-$Calb1^{tm2.1(cre)Hze}$/J	The Jackson Laboratory	RRID: IMSR_JAX:028532
Mouse: VGLUT2Cre; B6J.129S6(FVB)-$Slc17a6^{tm2(cre)Lowl}$/MwarJ	The Jackson Laboratory	RRID: IMSR_JAX:028863
Mouse: Gad2Cre; STOCK $Gad2^{tm2(cre)Zjh}$/J	The Jackson Laboratory	RRID: IMSR_JAX:010802
Mouse: VipCre; STOCK $VIP^{tm1(cre)Zjh}$/J	The Jackson Laboratory	RRID: IMSR_JAX:010908
Mouse: Tac1Cre; B6;129S-$Tac1^{tm1.1(cre)Hze}$/J	The Jackson Laboratory	RRID: IMSR_JAX:021877
Mouse: PenkCr; (B6;129S-$Penk^{tm2(cre)Hze}$/J	The Jackson Laboratory	RRID: IMSR_JAX:025112
Mouse: PacapCre; B6.Cg-$Adcyap1^{tm1.1(cre)Hze}$/ZakJ	The Jackson Laboratory	RRID: IMSR_JAX:030155
Mouse: tdTomato; B6;129S6-$Gt(ROSA)26Sor^{tm14(CAG-tdTomato)Hze}$/J; Ai14	The Jackson Laboratory	RRID: IMSR_JAX:007908
Software and algorithms		
LASX	Leica	RRID: SCR_013673
FIJI	[62]	RRID: SCR_002285
Prism 9	Graphpad	RRID: SCR_002798
Excel 2019	Microsoft	RRID: SCR_016137
Python (custom code)	This paper	DOI: 10.5281/zenodo.6976066

REAGENT or RESOURCE	SOURCE	IDENTIFIER
TomoPy	[56]	RRID:SCR_021359
Knossos	[57]	RRID:SCR_003582